Research Article

Ultra-low-loss all-fiber orbital angular momentum mode-division multiplexer based on cascaded fused-biconical mode selective couplers

Huiyi Guo, Yan-ge Liu,* Liang Chen, Wenzhe Chang [ID], Zekun Shi, Letian Gu, and Zhi Wang
Nankai University, Institute of Modern Optics, Tianjin Key Laboratory of Micro-scale Optical Information Science and Technology, Tianjin, China

Abstract. Mode-division multiplexers (MDMUXs) play a pivotal role in enabling the manipulation of an arbitrary optical state within few-mode fibers, offering extensive utility in the fields of mode-division multiplexing and structured optical field engineering. The exploration of MDMUXs employing cascaded resonant couplers has garnered significant attention owing to their scalability, exceptional integration capabilities, and the anticipated low insertion loss. In this work, we present the successful realization of high-quality orbital angular momentum MDMUX corresponding to topological charges 0, ±1, and ±2, achieved through the utilization of cascaded fused-biconical tapered couplers. Notably, the measured insertion losses at 1550 nm exhibit remarkable minimal values: 0.31, 0.10, and 0.64 dB, respectively. Furthermore, the 80% efficiency bandwidths exceed 106, 174, and 174 nm for these respective modes. The MDMUX is composed of precision-manufactured high-quality mode selective couplers (MSCs). Utilizing a proposed supermode propagation method based on mode composition analysis, we precisely describe the operational characteristics of MSCs. Building upon this comprehensive understanding, we embark on a pioneering analysis elucidating the influence of MSC cascading order on the performance of MDMUXs. Our theoretical investigation substantiates that when constructing MDMUXs, MSCs should adhere to a specific cascading sequence.

Keywords: space-division multiplexing; all-fiber devices; orbital angular momentum.

1 Introduction

The orthogonal modes present in few-mode fibers (FMFs) introduce a new dimension with diverse applications, widely exploited in communication, sensing,[1,2] and optical field manipulation.[3–5] Unlike single-mode fibers (SMFs), FMFs accommodate multiple transverse modes due to their larger core size and higher refractive index difference. These modes ideally remain isolated from power cross talk, serving as independent and intrinsic channels for information transmission. This unique property positions mode-division multiplexing (MDM) as a strong candidate for addressing potential capacity limitations in next-generation communication technologies.[6–9]

In the field of communications, substantial research efforts have been focused on achieving orthogonal eigenmodes while concurrently mitigating cross talk.[10–14] Conversely, within the domain of structured optical fields, the aim revolves around accessing a wide array of optical states within space and effecting seamless transitions between these distinct optical configurations. Mode-division multiplexers (MDMUXs) emerge as a solution satisfying both of these requirements. An MDMUX consists of N inputs and a single output. Each input activates a specific mode at the output terminal, corresponding to a predefined set of bases within the optical state space. When multiple ports are activated simultaneously, the result is a hybrid mode.

Many MDMUXs have been extensively studied and practically demonstrated. Approaches, such as beam combiners and mode converters, employing phase plates or spatial light modulators, enable the direct excitation of spatial modes.[15,16] However, these methodologies require the inclusion of bulky optical components and may encounter increased insertion

*Address all correspondence to Yan-ge Liu, ygliu@nankai.edu.cn

losses as the number of modes increases. In contrast, multiplane light conversion techniques facilitate the efficient conversion of a single-mode input into the desired output mode ensemble. By skillfully integrating phase plates and lenses, it remains possible to construct MDMUXs with acceptable losses and reduced dimensions.[17–22] The insertion loss of MDMUX based on a multiphase plane has been as low as 2.6 dB, achieving orbital angular momentum (OAM) MDM with topological charges ranging from 0 to 5.[23]

Fiber-based MDMUXs have emerged as captivating methodologies, underpinned by their inherent low loss. Notably compact and robust, they offer the advantage of direct connectivity to transmission fibers. For instance, photon lanterns adiabatically amalgamate N SMFs into a solitary multimode fiber capable of accommodating N modes.[24–28] Noteworthy mode selectivity can be achieved through the utilization of distinct fibers. Photon lanterns have demonstrated the multiplexing of up to five mode groups with a typical insertion loss of 5 dB.[29] Nevertheless, their design principles and manufacturing processes present challenges due to their intricate structural nature.

An alternate approach involves the conversion of the fundamental mode within an SMF to higher-order modes within an FMF, facilitated by mode selective couplers (MSCs) in conjunction with cascading techniques for mode multiplexing. Research has shown the feasibility of multiplexing four mode groups by cascading six MSCs.[10] Cascaded MSC mode multiplexers, leveraging both side-polishing (SP) and fused-biconical taper (FBT) technologies, have exhibited efficacy. However, FBT-based MSCs have traditionally encountered a persistent issue of elevated insertion losses, frequently surpassing several decibels.[11–13] The insertion loss of an MDMUX that multiplexes three mode groups is 0.3 dB for LP_{01} mode, 1.5 dB for LP_{11} mode, and 3.2 dB for LP_{21} mode excitation at the wavelength of 1550 nm.[14] Meanwhile, cascaded MSC mode multiplexers founded upon SP demonstrate enhanced insertion loss performance.[30–32] By utilizing the optimized SP process, the MDMUX insertion loss of LP_{11} and LP_{21} reaches 2.5 and 1.9 dB, respectively.[33] Nonetheless, inherent losses exceeding 1 dB remain inescapable for those modes higher than LP_{11}, engendering more intricate processing steps and elevated costs. The field of space-division multiplexing anticipates the emergence of MDMUX characterized by low loss and high performance. Notably, recent advancements have witnessed the unveiling of ultra-low-loss MSCs rooted in FBT technology, showcasing losses below 0.2 dB.[34] This development provides a promising cornerstone for the realization of low-loss MDMUXs.

On the other hand, the cascading order has long remained a relatively unexplored aspect. With the advent of high-performance MSCs, identifying the optimal cascading sequence for effective MDM emerges as a pivotal inquiry. The schematic depiction of cascaded MSCs is provided in Fig. 1. Mode 1 is engendered within MSC1 and subsequently guided into MSC2 through the FMF port, wherein Mode 2 is generated. Consequently, the joint production of Mode 1 and Mode 2 materializes at the output of MSC2. It is pertinent to acknowledge that MSC2, positioned in the latter stage, undertakes the dual roles of mode conversion and mode combination. In this context, MSC2 necessitates the simultaneous preservation of robust throughput for Mode 1 while fulfilling its designated mode conversion function to ensure low-loss and high-quality output of both Modes 1 and 2.

Previous investigations have employed cascaded MSCs based on side-polished adhesive bonding and FBT technology,
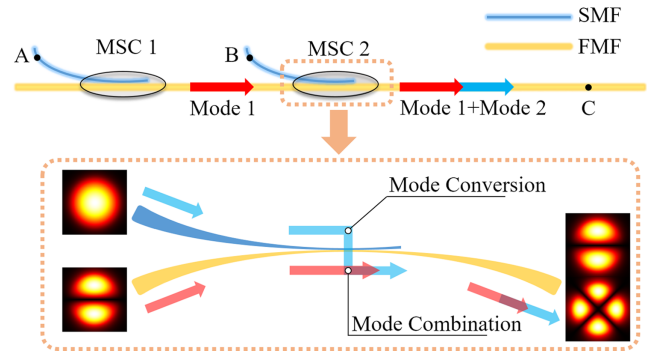

Fig. 1 Schematic diagram of cascaded MSCs.

arranging them from low-order to high-order modes. This approach seems intuitive, as low-order mode MSCs typically exhibit narrower taper waist dimensions, making them less suitable for transmitting high-order modes. Conversely, high-order modes possess larger taper waist diameters, allowing low-order modes to pass through with minimal cross talk. However, practical scenarios necessitate more nuanced deliberations, as the mode ordering within fibers is not universally consistent. In some instances, the intricate structures of FMFs utilized in MDM systems are customized to accommodate system capacity expansion, leading to changes in the mode ordering within the fiber, which deviates from uniformity.[35–38] Additionally, the mode order of tapered fibers diverges significantly from that of the original fiber. These nuanced situations introduce complexities in the realm of mode ordering within fibers. Consequently, further research is necessary to establish the guiding principles governing the optimal cascading order of MSCs.

In this paper, we embark on the fabrication of ultra-low-loss wideband FBT-MSCs and cascade them to achieve the multiplexing of OAM modes of orders 0, 1, and 2. This effort involves precise delineation of the geometric structure and refractive index distribution of MSCs, leveraging meticulous fiber parameters and advanced fabrication methodologies. We formulate and employ a supermode propagation method (SMPM) grounded in mode composition analysis to determine operational parameters for the MSCs. This approach facilitates the exploration of the optimal cascading sequence for the MSCs. Our experimentation verifies that achieving low cross talk hinges upon the uniqueness of the cascading sequence for MSCs targeting distinct modes. The empirical findings substantiate the effectiveness of cascaded MSCs in realizing the multiplexing of 0, 1, and 2 order OAM modes. At the wavelength of 1550 nm, the measured insertion losses remain impressively low: 0.31, 0.10, and 0.64 dB for the respective modes. Moreover, the 80% efficiency bandwidths exceed noteworthy thresholds of 106, 174, and 174 nm for these modes, respectively. Our research signifies achieving the lowest insertion loss for a three-order OAM mode MDMUX, to the best of our knowledge. This study unveils a comprehensive approach to employing cascaded FBT-MSCs for the realization of MDM, thereby serving as a notable blueprint for the design and fabrication of MDM devices founded on MSCs.

2 Supermode Propagation Method

The core operational region of the MSC comprises two closely juxtaposed uniform fiber tapers, encased within an air or another

isotropic homogeneous medium, as depicted in Fig. 2(a). Optical wave propagation occurs within this composite arrangement, involving both the fiber tapers and the surrounding medium. Given an incident field, the numerical computation method addresses the intricate dynamics of optical wave propagation within this composite configuration. In this context, classical coupled mode theory interprets this structure as two waveguides that mutually perturb each other slightly. This theory explicates the energy exchange between the eigenmodes of these waveguides during the transmission process, employing coupled mode equations. However, it is important to note that the coupled mode theory, rooted in perturbation principles, can yield distorted outcomes when dealing with waveguides situated in close proximity. This phenomenon arises due to the intensified interaction between the waveguides, which exerts a significant influence on the eigenmodes.

Here, we demonstrate an SMPM based on mode composition analysis, which can offer higher precision. The structure under simulation is fundamentally a longitudinally invariant waveguide, inherently possessing orthogonal eigenmodes. These eigenmodes exhibit self-replicating behavior as they propagate through the structure, manifesting solely as phase changes during transmission, eliminating the need to compute their modal field evolution. SMPM represents the input field as a linear superposition of supermodes (SMs), recording the phase changes of different SMs during transmission. These SMs

are then recombined at the output terminal with new phase relationships to yield the output field. Figures 2(b)–2(g) illustrate the typical procedural flow of this computational approach when taking the LP$_{11}$ MSC as an example. In Fig. 2(b), the composite structure is depicted both when treated as two distinct waveguides and as a composite waveguide. When this structure is treated as two separate waveguides, their eigenmodes are referred to as cylindrical vector (CV) modes; when this structure serves as a composite waveguide, its eigenmodes are referred to as cylindrical SMs. Both CV modes and SMs are calculated using the finite-element method. In Fig. 2(c), CV_1 serves as input mode $\mathbf{I}$ and is expressed as a summation of $\mathbf{SM}$s,

$$\mathbf{I} = \langle a | \mathbf{SM} \rangle, \tag{1}$$

where a is the complex amplitude vector whose elements are obtained by taking the inner product of $\mathbf{I}$ and $\mathbf{SM}$,

$$a_j = \langle \mathbf{I} | \mathbf{SM}_j \rangle^\dagger. \tag{2}$$

The amplitude and phase of a are depicted in Fig. 2(c). $\mathbf{SM}_1$ to $\mathbf{SM}_6$ possess distinct propagation constants, resulting in continually changing phase differences among different $\mathbf{SM}$ components as the transmission distance varies. Taking $\mathbf{SM}_1$ as the reference phase point, the phase differences between other $\mathbf{SM}$s and the reference point change with transmission distance,
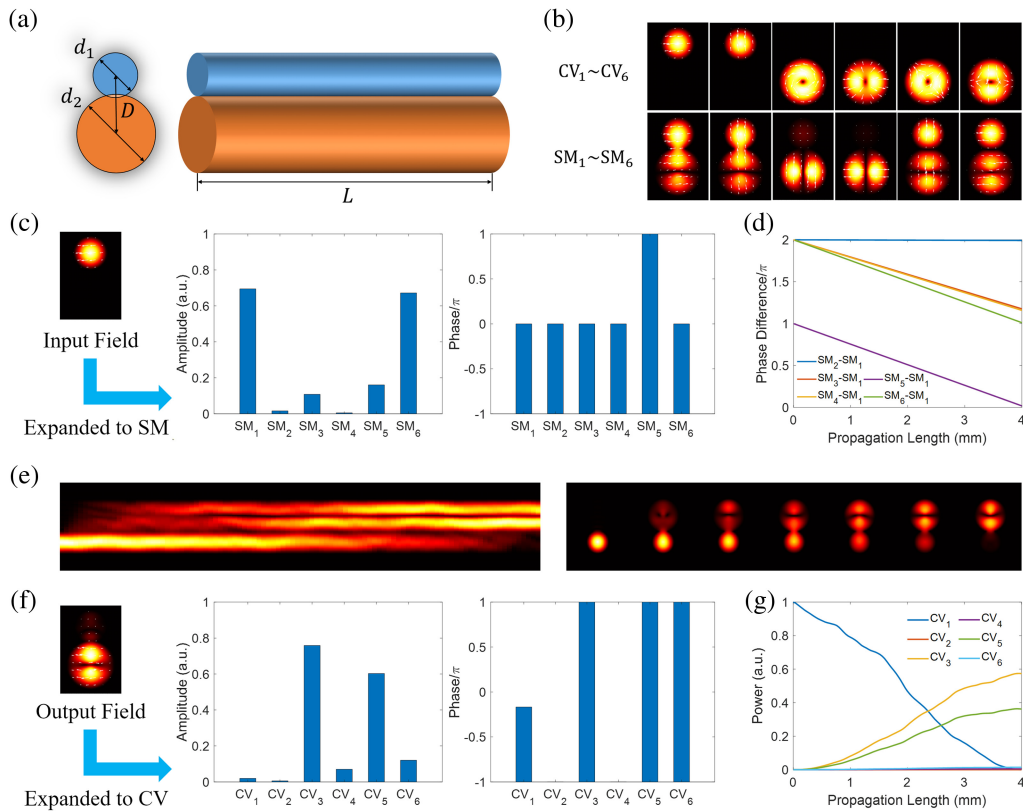
Fig. 2 SMPM algorithm flow. (a) Schematic illustration of the composite waveguide structure. (b) Mode patterns of CV modes and SMs. (c) Amplitude and phase spectra of the input mode expanded into SMs. (d) Variation of phase differences between SMs during transmission (with SM$_1$ as a reference). (e) Changes in mode field during transmission, side view, and slice view. (f) Amplitude and phase spectra of the output field expanded into CV modes. (g) Energy evolution of CV modes during transmission.

as illustrated in Fig. 2(d). Evidently, SM_2 and SM_1 have nearly identical propagation constants, yielding relatively constant phase differences between them. For other modes, phase differences with SM_1 linearly accumulate based on their respective propagation constants. Subsequently, at each transmission length, the SMs are combined using the initial complex amplitudes from Fig. 2(c) and the accumulated phase changes from Fig. 2(d), resulting in the output field O,

$$O = \langle a \circ \exp^{i\beta z}|SM\rangle, \tag{3}$$

where β represents the propagation constant vector of the SMs, and the symbol $\circ$ denotes the Hadamard product. The output fields O at different positions are calculated and shown in Fig. 2(e), including a side view and a cross-sectional view. Thus far, SMPM has provided the complete process of the transmission. Considering the focus is on the coupling process of CV modes, the output field O is expanded back to CV modes,

$$O = \langle b|CV\rangle, \tag{4}$$

where b represents the complex amplitude vector,

$$b_j = \langle O|CV_j\rangle^\dagger. \tag{5}$$

Figure 2(f) presents the amplitude spectrum and phase spectrum of the final output field expanded into CV modes. By expanding all the output fields O throughout the transmission process into CV modes, the power variations in terms of CV can be obtained, as shown in Fig. 2(g). In Eqs. (2) and (5), SM and CV should be complete to ensure that I and O can be fully expressed. Equivalently, the modulus of vectors a

and b should be equal to 1. In numerical calculations, it is sufficient to calculate SM and CV within a certain effective refractive index range. The specific form of the inner product between two modes, A and B, in the above equations is given as

$$\text{dot}_{AB} = \langle A|B\rangle^\dagger = \iint_\infty (A_x B_x^* + A_y B_y^* + A_z B_z^*)\mathrm{d}x\mathrm{d}y, \tag{6}$$

where A_x, A_y, and A_z represent the electric field components of mode A, and B_x, B_y, and B_z represent the electric field components of mode B. SMPM enables the investigation of the transmission characteristics of longitudinally invariant waveguides based on vector analysis. The computational complexity and precision of SMPM remain unaffected by the transmission length, and the algorithm does not rely on approximations or assumptions. In this study, SMPM is employed to aid in determining the operational state of MSCs and to meticulously analyze their transmission characteristics.

3 Fabrication and Accurate Model of MSCs

The refractive index profiles of single-mode and FMFs employed for MSC fabrication are depicted in Fig. 3(a), marked in red. The SMF features a negatively doped region situated between the core and cladding, while the FMF incorporates a positively doped region between the core and cladding. These distinctive profiles are designed to optimize the performance of the MSC while ensuring compatibility with conventional fibers.[34] The precisely characterized refractive index distribution aids in the accurate simulation of the MSC. The model utilized in simulations is a stepwise simplification based on the measured profiles, as depicted by the blue line in Fig. 3(a).
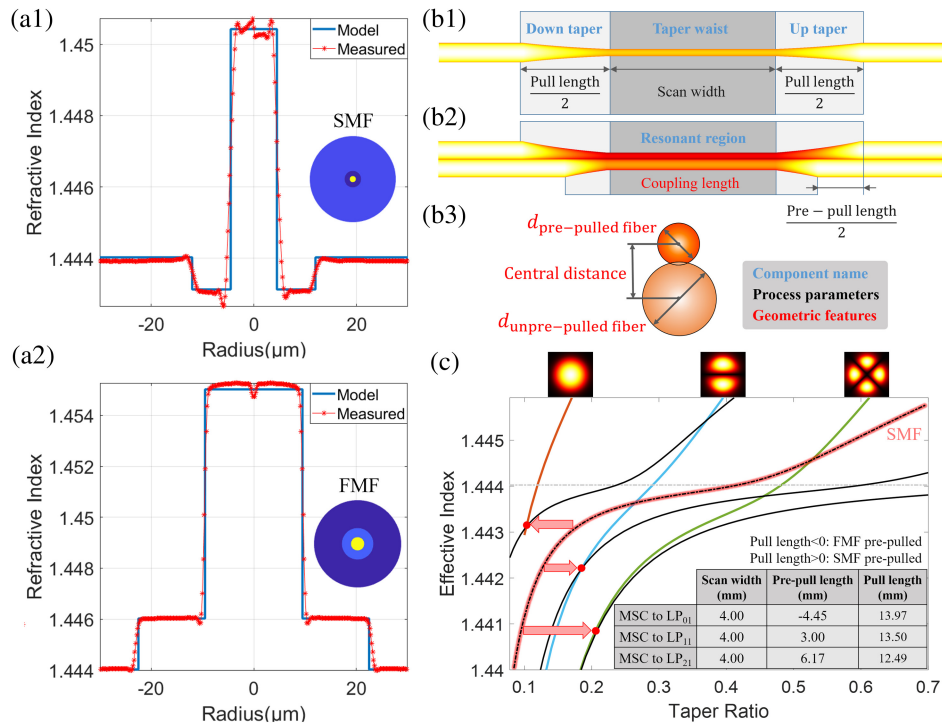
Fig. 3 (a1) and (a2) Refractive index profiles of SMF and FMF for MSC fabrication. (b1)–(b3) Schematic structures of the fiber taper and MSC. (c) TDCs for SMF and FMF, phase-matching points for MSC, and manufacturing parameters.

The manufacturing of MSCs relies on the FBT technique, which involves a dynamic heating process utilizing a swiftly moving flame brush and a slowly moving clamping device to achieve a quasi-static heating process. The process parameters and the tapered shape of the optical fiber adhere to a straightforward mapping relationship. Figure 3(b1) presents a schematic depiction of the tapered fiber's structure. The length of the uniform waist region of the tapered fiber, also known as coupling length, equals the width of the flame scan, while the total length of the upper and lower taper regions equals the pull length,

$$L_c = W_{\text{scan}}, \tag{7}$$

$$\text{Taper region length} = L_{\text{pull}}, \tag{8}$$

where L_c is the coupling length, L_{pull} represents the pull length, and W_{scan} is the flame scan width. The diameter of the taper waist region relative to the original fiber diameter is termed the taper ratio, and its value is derived from the principle of mass conservation,

$$\text{Taper ratio} = \exp\left(-\frac{L_{\text{pull}}}{2W_{\text{scan}}}\right). \tag{9}$$

An MSC is composed of two such parallel adjacent tapered fibers, as depicted in Fig. 3(b2). Coupled mode theory indicates that modes in two closely positioned waveguides can fully transform into each other at an appropriate coupling length when the phase-matching condition is met. The MSC operates based on this principle to generate the desired mode conversion. The source and target modes resonate in the taper waist for mode conversion, rendering this region the resonant area. To achieve mode resonance, controlling the taper waist diameter to meet the so-called phase-matching condition is necessary. As per Eq. (9), the desired taper waist diameter can be achieved by altering the pull length. Different pull lengths are required for SMF and FMF, achievable through pre-pull. Figure 3(b3) presents the geometric parameters of the resonant region of the MSC. The fiber's center-to-center spacing determines the degree of fusion (DoF) in the coupling region,

$$\text{DoF} = 1 - \frac{2D_c}{d_{\text{pp}} + d_{\text{upp}}}, \tag{10}$$

where D_c represents the center-to-center spacing, d_{pp} is the diameter of the pre-pulled taper waist, and d_{upp} is the diameter of the un-pre-pulled taper waist. In the FBT technique, DoF is positively correlated with the integral of the hot zone temperature over the processing period. The discussions above illustrate that FBT can determine the geometric configuration of the MSC, including coupling length, DoF, pre-pulled taper waist diameter, and un-pre-pulled taper waist diameter through fabrication parameters such as flame scan width, pull length, flame temperature, and heating time.

Based on the assumption that the refractive index profile during the fiber tapering process scales uniformly with the fiber diameter, the effective refractive index of the eigenmodes of the tapered waist is calculated for different taper ratios. This relationship is referred to as the tapered dispersion curve (TDC), which finds extensive use in the realm of mode-coupled devices.[39] Figure 3(c) illustrates the TDCs for both SMF and FMF. The colored curves represent FMF's LP_{01}, LP_{11}, and LP_{21} modes, while the black curve highlighted in red represents SMF's LP_{01} mode.

As previously mentioned, the manufacturing of the MSCs involves two tapering stages: pre-pull the SMF or FMF to establish the initial diameter ratio between two fibers, followed by a secondary tapering process where the diameter ratio remains constant to meet the preset phase-matching condition at the end of the process. The TDC aids in visualizing this process. Pre-pull SMF or FMF is equivalent to translating and scaling the TDC on the coordinate system. The translation and scaling of the TDC permit the target modes of SMF and FMF to intersect in the coordinate system. The intersection points on the TDC represent phase-matching points, indicating that the modes in SMF and FMF possess the same effective refractive index under the same taper ratio. A mature FBT process can accurately predict the fiber diameter at the taper waist, assisting in locating the phase-matching point. However, besides the phase-matching condition, the production of high-quality MSCs also relies on a proper match between coupling length and DoF. DoF cannot be easily predicted by processing parameters alone. Achieving an appropriate DoF necessitates iterative adjustments of the hot zone temperature and heating duration. Hence, the manufacturing parameters of MSCs are determined through iterative optimization during the fabrication process, as outlined in the table in Fig. 3(c). The flame scan width is set to 4 mm, and for MSCs targeting LP_{01}, LP_{11}, and LP_{21}, the pre-pull lengths are set at −4.45, 3.00, and 6.17 mm, respectively. The TDCs of the pre-pulled SMF are also plotted in Fig. 3(c), depicted by the black curve. The black curve intersects with FMF's LP_{01}, LP_{11}, and LP_{21} TDCs at the phase-matching points marked in red. Notably, when manufacturing the MSC for LP_{01} mode, the pre-pull length is specified as negative, indicating that SMF needs to be compressed along the length direction to achieve a larger initial diameter, causing the TDC to shift leftwards on the coordinate system. Considering that the crucial factor is the initial diameter ratio rather than the initial diameter, pre-pulling FMF is equivalent in the experiment. The manufactured MSCs exhibit ideal performance.[34] In subsequent discussions, MSCs targeting LP_{01}, LP_{11}, and LP_{21} modes are, respectively, labeled as MSC0, MSC1, and MSC2 for clarity.

To accurately simulate the operational state of the manufactured MSCs, it is crucial to possess a comprehensive understanding of their geometric characteristics. Of the four geometric parameters of MSCs, the coupling length L_c, diameter of SMF waist d_{SMF}, and diameter of FMF waist d_{FMF} are calculated based on processing parameters, and their values are listed in Fig. 4(a), whereas the DoF lacks a quantitative mapping relationship with processing parameters, rendering it inaccessible to direct determination. Furthermore, due to measurement limitations, practical measurement of DoF is also unfeasible. However, fortunately, since the manufactured MSCs achieve complete mode conversion at the coupling length, DoF can be numerically inferred in reverse. Figure 4(b) displays the coupling lengths at which mode conversion occurs for MSC0, MSC1, and MSC2 at different DoF values. A negative correlation between coupling length and DoF is observed, which intuitively aligns with stronger coupling requiring shorter coupling length. We adopt the DoF value corresponding to a coupling length of 4 mm as the model value for these MSCs, as indicated by the arrows in Fig. 4(b). The inset in Fig. 4(b) depicts the schematic of the MSCs model, with fiber diameters and DoF
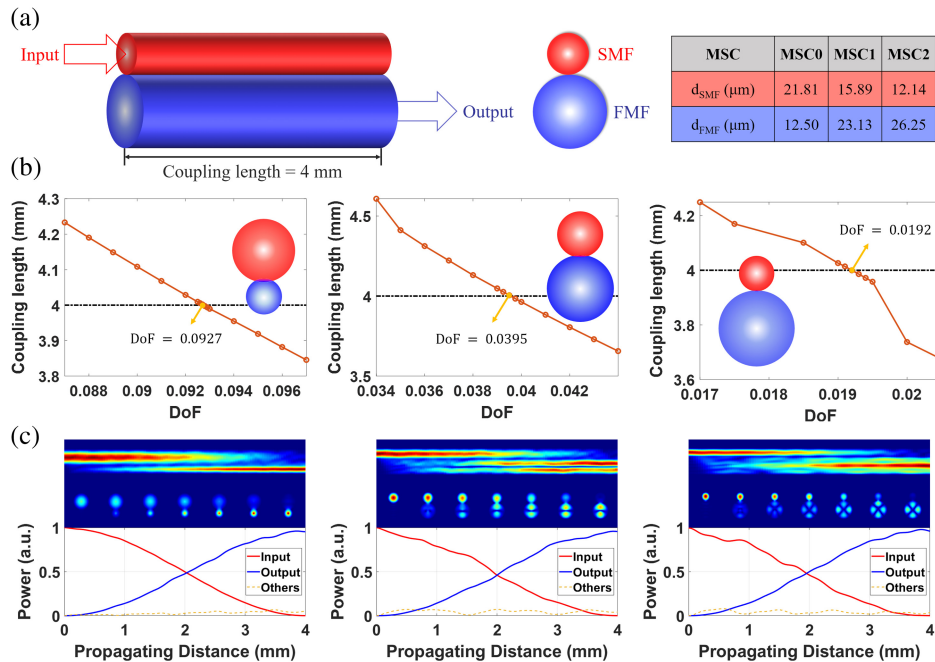
Fig. 4 Process for determining DoF. (a) Coupling lengths and taper diameters of MSC0, MSC1, and MSC2. (b) Variation of coupling length with DoF. (c) Simulation of the mode conversion process in MSCs.

illustrated to scale. With this, we established the digital models of the manufactured MSCs. Figure 4(c) illustrates the side views, cross sections, and mode power evolution of these MSCs when an SMF input is subjected to complete power mode conversion.

4 Permissible Cascading Order of MSCs

MSCs are assembled into an MDMUX through cascading. As shown in Fig. 1, the later-stage MSCs need to perform both mode conversion and mode combination simultaneously, leading to a specific order of arrangement that is not arbitrary. By qualitative discussions based on coupled mode theory and quantitative calculations using the proposed SMPM, the permissible cascading order can be clearly determined.

Through the satisfaction of phase-matching conditions and the matching of coupling length with DoF, MSCs have already demonstrated efficient mode conversion capabilities, as mentioned earlier. What we now need to address is whether the input modes from the preceding stage can pass through the current MSC without coupling, thus achieving mode multiplexing. Coupled mode theory indicates that the strength of coupling is related to the effective refractive index difference (also known as the phase mismatch factor) and the degree of mode field overlap. Specifically, smaller phase mismatch and greater mode field overlap promote coupling. In the composition of MSCs, both the SMF and the FMF support various modes in the coupling region. Among them, the SMF's LP_{01} mode, serving as the input mode, shares the same effective refractive index as the target mode in the FMF, as shown in Fig. 5(a). Furthermore, the SMF also supports several higher-order modes, while the FMF supports various lower-order and higher-order modes. When non-target modes from the FMF pass through the MSC, lower-order modes of the FMF often lack the SMF modes that phase-match with them. In contrast, the higher-order modes of the FMF have

an effective refractive index similar to the higher-order modes in the SMF. On the other hand, higher-order modes typically have larger evanescent fields, which further promote coupling. Therefore, lower-order modes are more likely to pass through the MSC without coupling, while higher-order modes are more likely to couple with the higher-order modes in the SMF. It is essential to note that there is no guarantee that MSC is transparent to lower-order modes, and whether coupling occurs and coupling strength should be precisely determined through numerical calculations.

Figure 5(b) displays the energy-level structure between the SMF and FMF for MSC0–MSC2. In MSC0–MSC2, the SMF's LP_{01} modes align with the FMF's LP_{01}, LP_{11}, and LP_{21} modes, respectively. In MSC0, the effective index of the FMF's LP_{11} mode is close to the SMF's LP_{31} mode, while the FMF's LP_{21} mode is similar to the SMF's LP_{03} and LP_{51} modes in terms of the effective index. In MSC1, the FMF's LP_{21} mode has an effective index similar to the SMF's LP_{11} mode. These modes with similar effective indices are prone to coupling, leading to mode cross talk. It is worth noting that in the optical fibers shown in Fig. 5(b), the mode arrangement order is not consistent. Even for tapered optical fibers of different diameters derived from the same original fiber, the mode arrangement order can vary. For example, in traditional step FMFs, the typical case is that the effective refractive index of the LP_{21} mode is lower than that of the LP_{02} mode. However, when the FMF is tapered to a certain size, the effective refractive index of the LP_{02} mode decreases faster, resulting in a lower value than that of the LP_{21} mode. Therefore, the arrangement order of the LP_{21} and LP_{02} MSCs is undetermined, depending on the mode order corresponding to the FMF diameter in the LP_{21} and LP_{02} MSCs. This is why determining the cascading order of MSCs using a constant mode sorting approach is challenging.
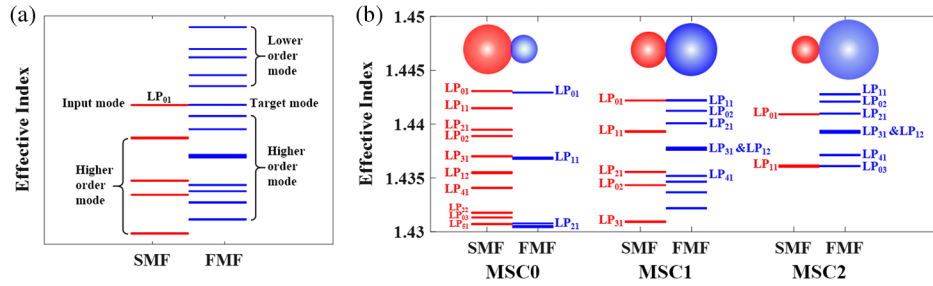
Fig. 5 (a) Schematic diagram of the energy-level structure of the coupling region in MSC. (b) The energy-level structure of SMF and FMF in MSC0–MSC2.

The quantitative analysis of transmittance for modes in the FMF is accomplished through the SMPM. The FMF input ports of the MSC0–MSC2 are injected with LP_{01}, LP_{11}, and LP_{21}, respectively, as illustrated in Fig. 6(a). The power output from the SMF port is referred to as loss, while at the FMF output port, the proportion of input mode power to total power is marked as purity. Clearly, an ideal cascading order should maintain low loss and high purity for the input modes, which determines the permissible cascading order of MSCs. Figures 6(c)–6(e) depict the evolution of mode fields and the variations in loss and mode purity when injecting LP_{01}, LP_{11}, and LP_{21} modes into the FMF input ports of MSC0–MSC2, respectively. The
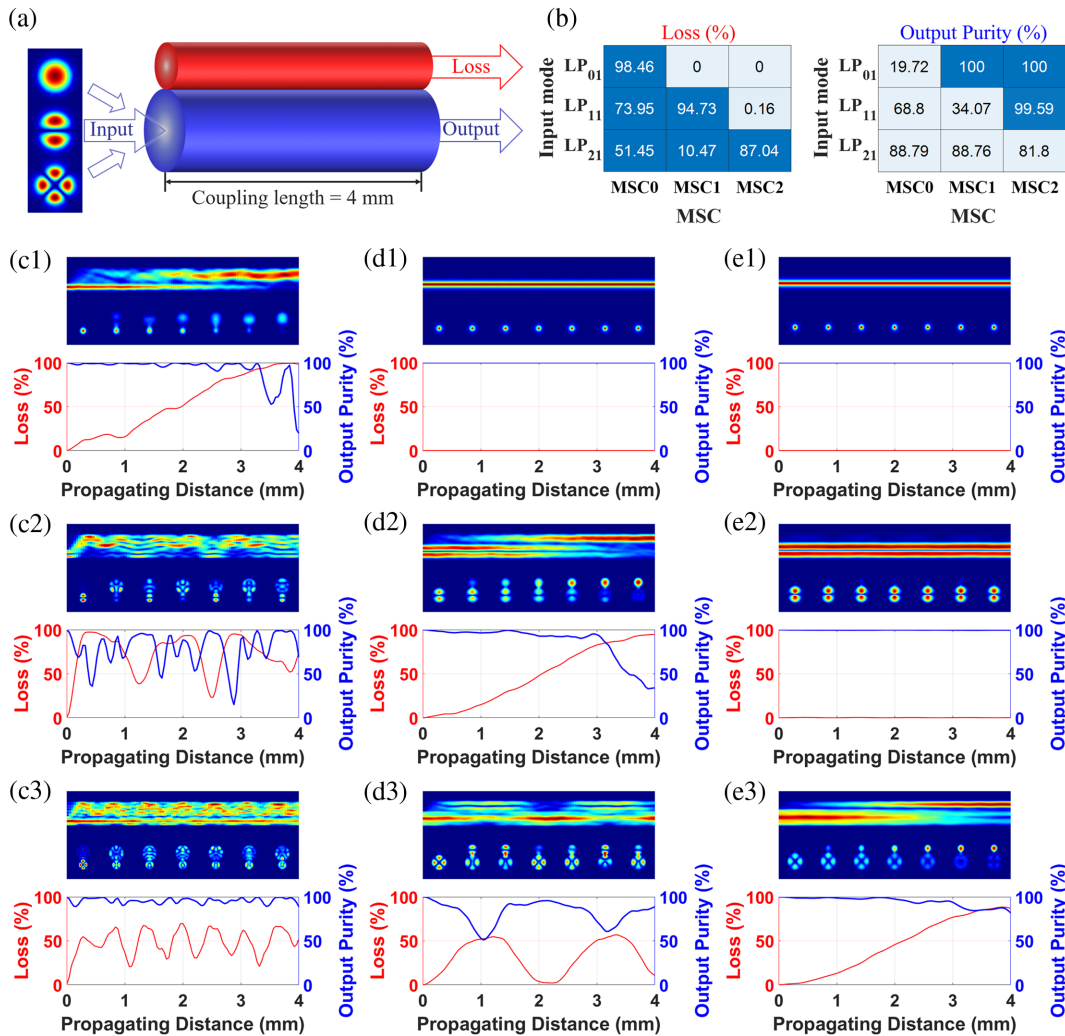
Fig. 6 (a) Schematic representation of the rear-stage MSC acting as a mode combiner. (b) Insertion loss and output mode purity after injecting different modes into MSCs. (c1–c3), (d1–d3), (e1–e3) Evolution of mode fields, along with changes in loss and purity, when injecting different modes into the FMF input port of MSC0–MSC2.

values of output loss and mode purity are presented in Fig. 6(b). All cases can be categorized into three groups: (1) c1, d2, and e3; (2) c2, c3, and d3; and (3) d1, e1, and e2. In cases c1, d2, and e3, the injected modes correspond to the output modes when the MSCs function as mode converters. In this scenario, the injected modes resonate with the fundamental mode in the SMF, resulting in clean mode coupling and high loss. In cases c2, c3, and d3, the injected modes experience chaotic coupling, leading to drastic changes in loss and mode purity, resulting in higher loss and poorer purity at the output. In cases d1, e1, and e2, the input modes hardly couple, achieving near 100% mode field purity and almost 0% loss at the output port. The simulation results indicate that MSC1 maintains a high throughput for the LP_{01} mode, while MSC2 maintains good throughputs for both LP_{01} and LP_{11} modes. Therefore, for assembling the MDMUX, the cascading order should be MSC0-MSC1-MSC2 to achieve optimal MDM performance.

5 Performance of MDMUX

To assess the performance of the cascaded MDMUX, a testing system for insertion loss and output mode characterization is established, as illustrated in Fig. 7(a). The light source is guided by optical switches to inject into the three input ports of the MDMUX, enabling the excitation of different modes. An imaging system with an interferometric optical path is set up at the output end of the MDMUX to facilitate mode observation and purity measurement. Power monitoring points (I0, I1, I2, and O) are designated at the input and output ends of the MDMUX for insertion loss testing. Polarization controllers PC0–PC2 are positioned after MSC0–MSC2 to adjust the phase difference within the mode groups to generate OAM modes.

The insertion loss test covers wavelengths ranging from 1465.00 to 1639.31 nm with a wavelength step of 0.01 nm. The purity test spans 1460 to 1640 nm, with a wavelength step

of 45 nm. The results of the insertion loss are presented in Fig. 7(b). Over the test wavelength range, the insertion loss remains below 3 dB, with I1 − O and I2 − O exhibiting good flatness and insertion losses below 0.6 and 0.8 dB, respectively. The insertion loss curve of I0 − O shows localized fluctuations, attributed to the presence of impurities generated by MSC0. These impurities result in power loss as the signal passes through MSC1 and MSC2. Table 1 provides the typical insertion loss and 80% efficiency bandwidth of the MDMUX. At 1550 nm, the insertion losses for zeroth- to second-order OAM modes are 0.31, 0.10, and 0.64 dB, respectively. The corresponding 80% bandwidths exceed 106, 174, and 174 nm, respectively.

The OAM mode is generated from the LP mode after undergoing birefringence with appropriate direction and optical path difference, which is achieved through adjusting PC0–PC2.[40] The rotation direction of the generated OAM depends on the sign of the optical path difference. The output OAM mode fields and interferometric vortices at different wavelengths are shown in Fig. 8. The purity of the modes at 1550 nm, with topological charges of 0, +1, −1, +2, and −2, is assessed using the mode composition analysis method shown in Refs. [41] and [42]. The purities are found to be 97.28%, 96.65%, 93.90%, 99.38%, and 96.22%, respectively. The correlation coefficients between the reconstructed mode fields and the measured mode fields are 97.29%, 98.47%, 99.03%, 97.26%, and 96.79%, respectively.

It is worth noting that during the fabrication of the MDMUX, the MSCs are manufactured compactly along a section of the FMF to avoid potential degradation in mode purity due to fusion splicing. Continuous manufacturing has posed challenges to the yield rate and cannot ensure that each MSC achieves its optimal performance. Under the premise of equipment and processing methods with good repeatability, the performance of MDMUX can reach a more ideal level.
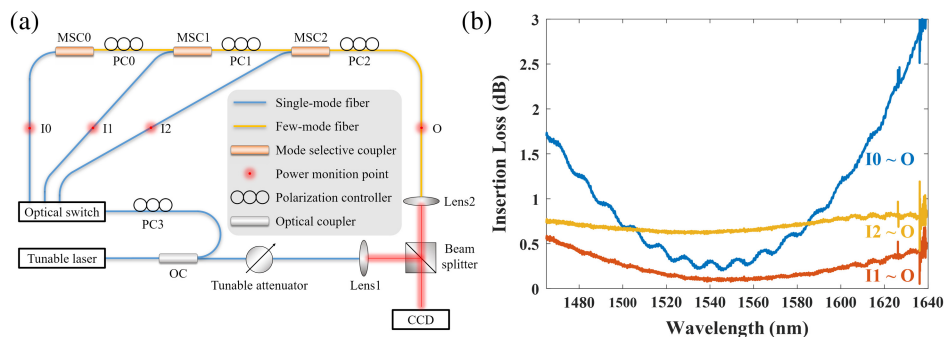

Fig. 7 (a) Experimental setup for MDMUX testing. (b) Measured insertion loss of the MDMUX. The fluctuations near 1635 nm are attributed to the instability of the light source.

Table 1 Insertion losses and 80% working bandwidth of the MDMUX.

OAM topological charge	Insertion loss @1550 nm (dB)	80% efficiency wavelength range[a] (nm)	80% efficiency bandwidth (nm)
0	0.31	1489–1595	106
±1	0.10	(1465)–(1639)	> 174
±2	0.64	(1465)(1639)	> 174

[a]Parentheses indicate the bandwidth out of the test band range
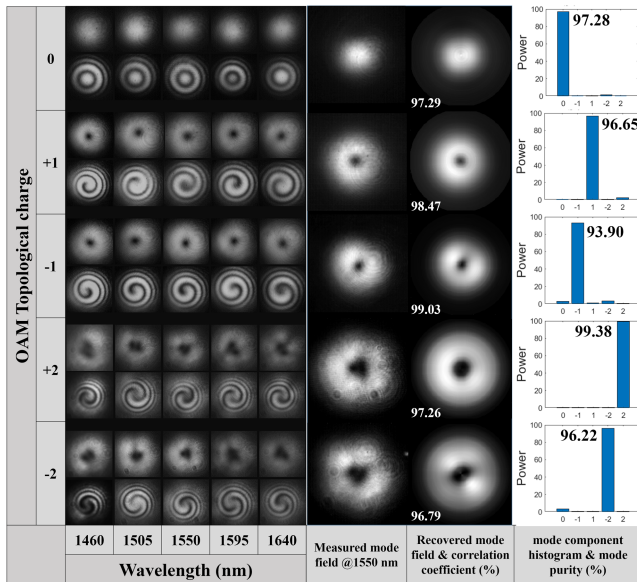
Fig. 8 Output OAM mode fields and interferometric vortices of the MDMUX with topological charges of 0, ±1, and ±2, analysis results of mode components at 1550 nm, as well as a comparison between the recovered mode field and the original mode field.

6 Conclusion

In this study, we have achieved an ultra-low-loss all-fiber MDMUX capable of multiplexing zeroth-, first-, and second-order OAM modes. The insertion losses were, remarkably, as low as 0.31, 0.10, and 0.64 dB at 1550 nm, respectively. Additionally, the 80% efficiency bandwidths exceeded 106, 174, and 174 nm, respectively. To the best of our knowledge, this represents one of the lowest insertion loss instances for a three-order OAM MDMUX. Benefiting from the precise refractive index distribution of optical fibers, robust fabrication techniques, and the proposed comprehensive vectorial SMPM simulations, we achieved accurate modeling of the manufactured MSCs. Moreover, we conducted a comprehensive analysis of the impact of cascading order on MSCs when utilized in cascaded MDM configurations. Our findings have established that for achieving low cross talk in cascaded systems, the cascading order of MSCs targeting different modes must adhere to a unique sequence. This work has illuminated the comprehensive process of utilizing cascaded FBT-MSCs to realize MDM functionality, setting an exemplary paradigm for the design and fabrication of MDM devices based on MSCs.

Disclosures

The author declares that there is no conflict of interest.

Code and Data Availability

All data in support of the findings of this paper are available within the article or as supplementary material.

References

1. K. Li et al., "Ultrasensitive optical microfiber coupler based sensors operating near the turning point of effective group index difference," *Appl. Phys. Lett.* **109**(10), 101101 (2016).
2. C. Caucheteur et al., "Mode-division and spatial-division optical fiber sensors," *Adv. Opt. Photonics* **14**(1), 1–86 (2022).
3. R. Zhu et al., "Virtual metasurfaces: reshaping electromagnetic waves in distance," *Photonics Res.* **11**(2), 203 (2023).
4. M. Cao et al., "Cylindrical vector beams demultiplexing communication based on a vectorial diffractive optical element," *Nanophotonics* **12**(9), 1753–1762 (2023).
5. K. He et al., "Polarization-dependent reconfigurable light field manipulation by liquid-immersion metasurface," *Opt. Express* **31**(9), 13739 (2023).
6. J. Du et al., "Mode division multiplexing: from photonic integration to optical fiber transmission [Invited]," *Chinese Opt. Lett.* **19**(9), 091301 (2021).
7. B. J. Puttnam, G. Rademacher, and R. S. Luís, "Space-division multiplexing for optical fiber communications," *Optica* **8**(9), 1186 (2021).
8. D. J. Richardson, J. M. Fini, and L. E. Nelson, "Space-division multiplexing in optical fibres," *Nat. Photonics* **7**(5), 354–362 (2013).
9. G. M. Saridis et al., "Survey and evaluation of space division multiplexing: from technologies to optical networks," *IEEE Commun. Surv. Tuts.* **17**(4), 2136–2156 (2015).
10. S. H. Chang et al., "All-fiber 6-mode multiplexers based on fiber mode selective couplers," *Opt. Express* **25**(5), 5734 (2017).
11. J. Li et al., "Prototype of DSP-free IM/DD MDM transceiver for datacenter interconnection," *J. Lightwave Technol.* **40**(5), 1283–1295 (2022).
12. Y. Gao et al., "Prototype system for real-time IM/DD MDM transmission based on multiple-ring-core FMF and degenerate-mode-selective reception," *Opt. Express* **27**(26), 38281 (2019).
13. Y. Gao et al., "A degenerate-mode-selective coupler for stable DSP-free MDM transmission," *J. Lightwave Technol.* **37**(17), 4410–4420 (2019).
14. F. Ren et al., "Three-mode mode-division-multiplexing passive optical network over 12-km low mode-crosstalk FMF using all-fiber mode MUX/DEMUX," *Opt. Commun.* **383**, 525–530 (2017).
15. R. Ryf et al., "Mode-division multiplexing over 96 km of few-mode fiber using coherent 6×6 MIMO processing," *J. Lightwave Technol.* **30**(4), 521–531 (2012).
16. M. Salsi et al., "Mode-division multiplexing of 2 × 100 Gb/s channels using an LCOS-based spatial modulator," *J. Lightwave Technol.* **30**(4), 618–623 (2012).
17. J. F. Morizur et al., "Efficient and mode-selective spatial multiplexer based on multi-plane light conversion," in *Opt. Fiber Commun. Conf. OFC*, Vol. 22, pp. 488–496 (2015).
18. G. Labroille et al., "Mode selective 10-mode multiplexer based on multi-plane light conversion," in *Opt. Fiber Commun. Conf. Exhibit. OFC*, pp. 10–12 (2016).
19. N. Barré et al., "Broadband, mode-selective 15-mode multiplexer based on multi-plane light conversion," in *Opt. Fiber Commun. Conf. OFC*, pp. Th2A-7 (2017).
20. J. Fang et al., "Performance optimization of multi-plane light conversion (MPLC) mode multiplexer by error tolerance analysis," *Opt. Express* **29**(23), 37852 (2021).
21. A. Kong et al., "Extending orbital angular momentum multiplexing to radially high orders for massive mode channels in fiber transmission," *Opt. Lett.* **48**(14), 3717–3720 (2023).
22. K. Ong et al., "Performance optimization of multi-plane light conversion (MPLC) mode multiplexer by error tolerance analysis," *Opt. Express* **29**(23), 37852–37861 (2021).
23. J. U. F. Ang et al., "Optical orbital angular momentum multiplexing communication via inversely-designed multiphase plane light conversion," *Photonics* **10**(9), 2015–2023 (2022).

24. S. G. Leon-Saval, A. Argyros, and J. Bland-Hawthorn, "Photonic lanterns," *Nanophotonics* **2**(5–6), 429–440 (2013).
25. Y. Wang et al., "Design of elliptical-core five-mode group selective photonic lantern over the C-band," *Opt. Express* **27**(20), 27979 (2019).
26. S. G. Leon-Saval et al., "Mode-selective photonic lanterns for space-division multiplexing," *Opt. Express* **22**(1), 1036 (2014).
27. H. Wang et al., "6-mode and 10-mode photonic lantern mode multi/demultiplexers based on silica planar lightwave circuit," *Opt. Commun.* **529**, 129098 (2023).
28. J. J. Davenport et al., "Photonic lanterns: a practical guide to filament tapering," *Opt. Mater. Express* **11**(8), 2639 (2021).
29. A. M. Velázquez-Benítez et al., "Scaling photonic lanterns for space-division multiplexing," *Sci. Rep.* **8**(1), 8897 (2018).
30. K. J. Park et al., "All-fiber mode division multiplexer optimized for C-band," in *Opt. Fiber Commun. Conf. OFC 2014*, pp. 5–7 (2014).
31. K. J. Park et al., "Broadband mode division multiplexer using all-fiber mode selective couplers," *Opt. Express* **24**(4), 3543 (2016).
32. K. Zhang et al., "Broadband mode-selective couplers based on tapered side-polished fibers," *Opt. Express* **29**(13), 19690 (2021).
33. J. Cui et al., "Five-LP-Mode IM/DD MDM transmission based on degenerate-mode-selective couplers with side-polishing processing," *J. Lightwave Technol.* **41**(10), 2991–2998 (2023).
34. H. Guo et al., "Ultra-low-loss 5-LP mode selective coupler based on fused biconical taper technique," *Opt. Express* **31**(11), 18050 (2023).
35. S. Matsuo et al., "Recent progress on multi-core fiber and few-mode fiber," in *Opt. Fiber Commun. Conf. OFC 2013*, pp. 3–5 (2013).
36. H. Kubota and T. Morioka, "Few-mode optical fiber for mode-division multiplexing," *Opt. Fiber Technol.* **17**(5), 490–494 (2011).
37. J. Li et al., "Geometric structure optimization of the ring-core fiber for high-order cylindrical vector beam modes transmission," *Opt. Commun.* **470**, 125761 (2020).
38. H. Li et al., "Optical property of few-mode fiber with non-uniform refractive index for cylindrical vector beam generation," *Proc. SPIE* **10153**, 101530K (2016).
39. S. Jiang et al., "Ultra-low-loss broadband all-fiber mode selective couplers for MIMO-Less MDM transmission," *J. Lightwave Technol.* **38**(8), 2376–2382 (2020).
40. Y. Han et al., "Controllable all-fiber generation/conversion of circularly polarized orbital angular momentum beams using long period fiber gratings," *Nanophotonics* **7**(1), 287–293 (2018).
41. Z. Shi et al., "Accurate and noise-robust mode decomposition by analyzing the intensity distribution of a few-mode ring core fiber," *J. Lightwave Technol.* 1–11 (2023).
42. Z. Shi et al., "Accurate mode purity measurement of ring core fibers with large mode numbers from the intensity distribution only," *Photonics Res.* **11**(9), 1592–1605 (2023).

Huiyi Guo received his BS degree in optical information science and technology from Nankai University, Tianjin, China, in 2018. He is currently working toward a PhD in optical engineering at the Institute of Modern Optics, Nankai University. His research interests are primarily focused on fiber coupling devices and micro/nanostructured optical fiber devices.

Yan-ge Liu received her MS degree in optics from Nankai University, Tianjin, China, in 1998 and her PhD in optic engineering from Tianjin University, Tianjin, in 2001. She is currently a professor at the Institute of Modern Optics, Nankai University. Her research interests include photonic crystal fiber/hollow core fiber/few-mode fiber and their applications, micro/nanostructured optical fiber devices, optical fiber communication and sensing technology, and optical fiber lasers and amplifiers. She has authored or co-authored more than 150 peer-reviewed journal papers, with total citations of more than 5000.

Liang Chen received his BS degree in optical information science and technology from Harbin Engineering University, Harbin, China, in 2020. He is currently working toward a PhD in optical engineering at the Institute of Modern Optics, Nankai University. His research interests are primarily focused on fiber coupling devices and micro/nanostructured optical fiber devices.

Wenzhe Chang received her BS degree in optics and electronics in science and engineering from Ocean University of China, Qingdao, China, in 2019. She is currently working toward the master's degree in optical engineering at the Institute of Modern Optics, Nankai University. Her research interest is on the fabrication of mode converters.

Zekun Shi received his BS degree in physics from Jilin University, Changchun, China, in 2021. He is currently working toward a PhD in optical engineering at the Institute of Modern Optics, Nankai University. His research interests are mainly focused on spatial modes in fiber.

Letian Gu received his BS degree in optical information science and technology from Nankai University, Tianjin, China, in 2022. He is currently working toward a PhD in optical engineering at the Institute of Modern Optics, Nankai University. His research interests are primarily focused on the pattern characteristic of structured light in few-mode fiber.

Zhi Wang received his PhD in optics from Nankai University, Tianjin, China, in 2005. He is currently a professor at the Institute of Modern Optics, Nankai University. His research interests include photonic crystal fiber or multimode fiber mode control theory, micro or nanostructured fiber sensing technology, ultrafast fiber laser technology, nonlinear fiber optics, and nonlinear space-time dynamics of multimode fiber.